Powder Technology 469 (2026) 121804

Contents lists available at ScienceDirect

Powder Technology

journal homepage: www.journals.elsevier.com/powder-technology

DEM simulations and PEPT measurements of the dynamics of dry mixing NMC 622 cathode material in an Eirich mixer

S.D. Hare [a,*], C. Lischka [b], J. Grogan [a], D. Werner [a], H. Nirschl [b], E. Kendrick [c], C.R.K. Windows-Yule [a], M.J.H. Simmons [a]

[a] School of Chemical Engineering, University of Birmingham, Edgbaston, Birmingham, B15 2TT, UK
[b] Institute of Mechanical Engineering and Mechanics, Karlsruhe Institute of Technology, Karlsruhe, Germany
[c] School of Metallurgy and Materials, University of Birmingham, Edgbaston, Birmingham, B15 2TT, UK

GRAPHICAL ABSTRACT

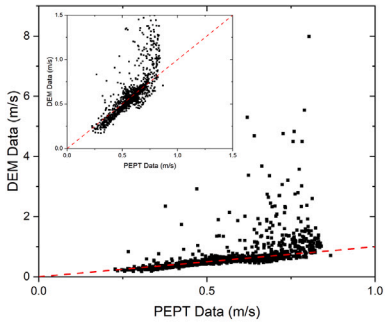

DEM simulation validated using PEPT experimental data

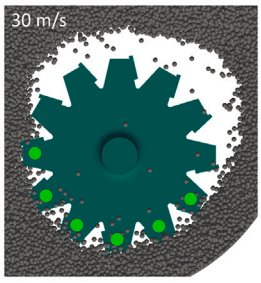

Material free surface pulls away from internal rotor as tip-speed increases

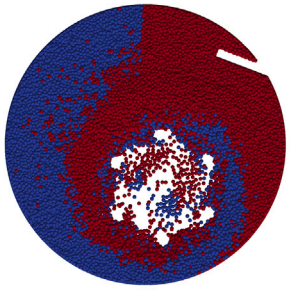

Transient mixing time shows higher tip-speed only marginally increases performance

HIGHLIGHTS

- Dry mixing of a cathode material simulated using the Discrete Element Method (DEM).
- DEM simulation experimentally validated using Positron Emission Particle Tracking (PEPT).
- Both DEM and PEPT show material surface pulling away from rotor at higher tip-speeds.
- Transient mixing time shows limited gains in mixing performance with higher tip-speeds.

ARTICLE INFO

Keywords:
Positron Emission Particle Tracking (PEPT)
Discrete Element Method (DEM)
Lithium-ion battery
Simulation validation
Cathode

ABSTRACT

Understanding of dry mixing of battery electrode materials has the potential to improve process sustainability by elimination of organic solvents, as well as the energy costs of slurry drying. The dry mixing dynamics of NMC 622, a cathode electrode material used in lithium-ion batteries, were obtained experimentally in an Eirich mixer using Positron Emission Particle Tracking (PEPT); the results were compared with simulations using the Discrete Element Method (DEM). The internal rotor tip speed was altered between 10, 20 and 30 m/s, with

* Corresponding author.
E-mail address: s.d.hare@bham.ac.uk (S.D. Hare).

https://doi.org/10.1016/j.powtec.2025.121804
Received 23 June 2025; Received in revised form 20 October 2025; Accepted 22 October 2025
Available online 27 October 2025

NMC 622

the rotational speed of the co-rotating outer mixing pan kept constant at 0.7 m/s. Depth-averaged heat maps of velocity obtained from PEPT were compared with DEM, focusing on key features of the mixer, namely the internal rotor, rotating pan wall and wall-scraper. Both PEPT and DEM data showed that the velocities were highest close to the rotor, and then dropped towards the wall-scraper, which disrupts material flow and improves dispersion. At the wall edge the velocity was constant due to the unchanged rotating motion of the pan. Both methods also capture a previously unobserved disengagement of the free surface of the electrode material from the rotor at higher tip-speeds, diminishing mixing performance, confirmed by estimating the transient mixing time using the Lacey mixing index. The gains in mixing performance are thus shown to have diminishing returns with increasing tip-speed, suggesting that mixing at lower speeds may, for the materials investigated here, prove more economical and thus more environmentally sustainable.

1. Introduction

With the push towards electrification of vehicles [1], and the need for more renewable energy sources, the demand for batteries to enable this change is expected to grow dramatically, due in part to large-scale battery storage to smooth out the variability of renewable sources [2]. With this rapid increase in the demand for batteries, the supply chain of the critical materials used to manufacture Lithium-ion batteries will become strained as many of the required materials will need to be mined [3]. This strengthens the crucial need to understand the use of materials for existing and new battery chemistries [4], as well as how to improve the recycling efforts for end-of-life cells [5]. In addition, it is very important to be able to manufacture in an efficient way and also to bring new products and technologies to market with a minimum of trials and waste, especially as scale tends to bring about significant energy savings [6]. This may help to lower the substantial energy costs in the slurry casting process by which battery electrodes are made, particularly in the drying step [7]. Increasing solids-content of slurries yields potential energy savings of approximately 7% and moving to a dry mixing process, approximately 18 % [8]. Furthermore, as the energy mix used in production becomes more renewable, dry coating technologies are highly ranked on potential emissions savings [9].

Lithium-ion battery manufacturing is a complex multistep process, with each step requiring precise results to ensure both the final electrochemical performance and the processability for each subsequent downstream process [10]. Consequently, there is considerable academic and industrial interest in developing improved metrology and modelling approaches to enable the early detection of manufacturing defects that can cascade through the manufacturing process and impact final electrode performance. In addition to improving existing manufacturing practice, this would also accelerate the development of new formulations and processes, such as the development of water-based binders for cathode slurries [11], solvent-free mixing [12,13], introduction of solid electrolytes [14], and lead to improved mixing procedures to optimise the rheology and microstructure of the slurry [15,16].

The mixing of particulate and liquid components is a critical first step in the formation of a battery electrode slurry. It is typically carried out in a batch mixer, following a precise, yet empirically optimised recipe after which the slurry is coated onto a metal film substrate. As mentioned above, removal of solvent is a potential way of vastly reducing energy costs and required factory footprint. To date, dry mixing of particulate electrode components before addition of solvent in a wet slurry process has been shown to be beneficial in creating a preferential distribution of the conductive additive onto the surface of the active material [17–19], improving final cell performance. There is potential for this methodology to be extended to eliminate the solvent entirely. However, before this operation can be explored, it is necessary to generate an understanding of the dynamics of this process and the relationships between the operating parameters of the batch mixer, the mixing performance and ultimately how these impact the electrochemical performance. As an example, for NMP-PVDF slurries, the carbon black conductive additive forms a weak network that stabilises the slurry [20], so a balance must be struck between coating the conductive additive onto the surface of the active material [21] and leaving enough free to both stabilise the slurry after coating, and to form the crucial 3D conductive network once dried and calendared [22].

Many different types of batch mixers are employed at different scales in the manufacturing of Li-ion batteries, including hand grinding, homogenisers, planetary mixers, ball mills, and high shear mixers [23–27]. Some designs have the ability to mix wet and dry, and others are known to possess issues with scalability, or only excel in one aspect or component of slurry mixing. The Eirich mixer, which uses an eccentric impeller with a rotating pan and wall-scraper, has emerged as a popular choice now widely used within industry (e.g. UK Battery Industrialisation Centre https://www.ukbic.co.uk) due to its availability at scales ranging from 0.1–12,000 L in capacity. This mixer design is thus the focus of this research to test its applicability and capability for dry mixing.

This paper describes an experimental and numerical investigation of how the dynamics of dry-blending of NMC 622, a commonly used cathode material in Li-ion batteries, are affected by changing speed of the internal rotor in an Eirich EL1 0.3–1 L capacity mixer, from the point of view of industrial optimisation. The Eirich mixer differs from classic stirred tanks due to its rotating pan (run co-current or counter-current to the rotor) and wall-scraper, as well as operating at lower fill heights. These design changes alongside the off centre, eccentric impeller lead to substantial changes to mixing dynamics when compared to simpler mixers. The velocity of the powder in the mixer is measured experimentally using positron emission particle tracking (PEPT), a nucleonic method which enables a variety of measurements concerning particle velocity, residence time, mixing dynamics and a variety of other key dynamical properties to be made in opaque materials via tracking of a single radioactive tracer particle of similar properties to the powder [28,29]. These are the first experimental flow measurements made for dry blending of electrode materials in a batch system. Other typical constituents of LiB electrodes such as binder or conductive additives were not included in this study since these tend to influence the bulk behaviour significantly over time which was shown in prior work [21,30], which would lead to a time-evolving change in particle properties which could not be captured using the techniques available. The experimental results are compared with values obtained from Discrete Element Method (DEM) simulations, as a route to future digital optimisation of mixer parameters.

2. Experimental

2.1. Mixer design

An Eirich EL1 mixer (nominal capacity 0.3–1 L) equipped with a Z-type rotor was used, at rotor tip-speeds of 10 m/s (2300 rpm), 20 m/s (4600 rpm) and 30 m/s (6900 rpm), which were set to co-rotate with the mixing pan, rotating at a constant speed of 0.7 m/s (85 rpm). The tool speed of 30 m/s reflects the highest possible energy input in the EL1 mixer. Earlier experimental work [21] with the same NMC 622 cathode material showed via SEM imaging that even for long mixing times of up to 90 min no significant particle breakage of the active material is detectable. 3D models of the mixer and rotor geometry are shown in Fig. 1. The mixer was filled with 0.7 kg of NMC 622 with particle size fractions of D_{50} = 10 μm, D_{10} = 5.5 μm and

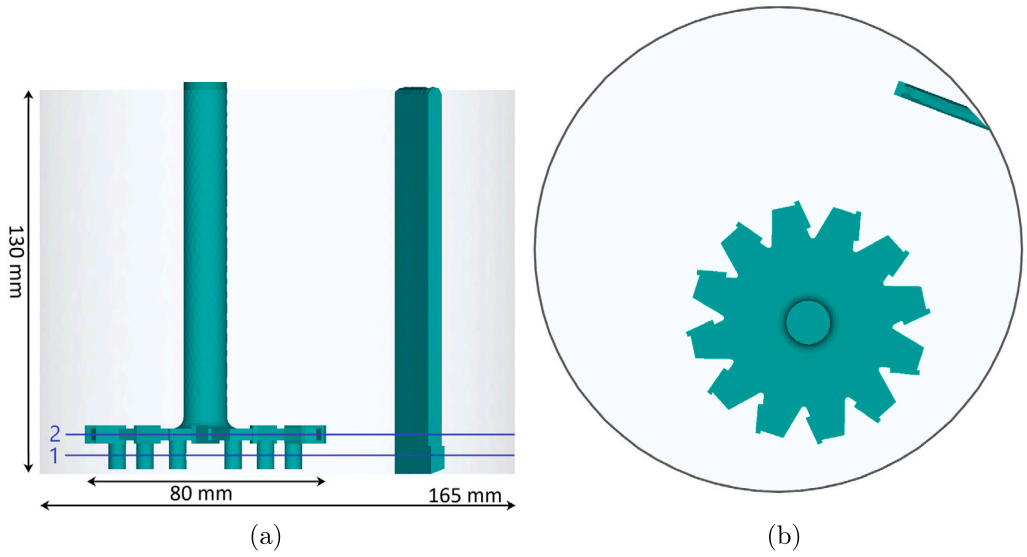

Fig. 1. Side on (a) and top-down (b) view of the Eirich EL1 mixer. The blue lines labelled 1 and 2 in (a) denote the planes along which granular temperature is calculated.

D_{90} = 17 μm, and a solids density of ρ_p = 4650 kg/m^3. When compared to a conventional stirred tank, the fill height (25 mm) is low, due to the mixing pan being wider (165 mm) than it is tall (130 mm), to accommodate the option to angle the pan for other mixing/granulation processes.

2.2. PEPT measurements

Since PEPT relies on the movement of a single radioactive tracer particle which emits highly penetrative back-to-back gamma rays, it can be used in opaque equipment (i.e. metal) and media. PEPT has been applied to a wide variety of industrially relevant mixing systems, including coffee roasters [31], stirred tank reactors [32,33], ball mills [34], fluidised beds [35], and others [36].

In addition to providing valuable information in its own right, PEPT can also be used as a means validating numerical models, including discrete element method [37], computational fluid dynamics [38], and other [39,40] simulations. The ability of PEPT data to be analysed to produce many of the same three-dimensional fields as, for example, DEM, enables detailed, three-dimensional comparisons between experimental and numerical data to be made across a range of relevant properties, thus facilitating a uniquely rigorous form of validation for rapidly-flowing particulate systems.

The tracer particle used was an ion-exchange resin bead, approximately 300 μm in size, approximately 30x larger than the individual NMC 622 particles (10 μm), but approximately 10x smaller than the coarse-grained DEM particles (2 mm). The tracer was labelled with the β^+-emitting radioisotope Fluorine-18. This labelling process involved immersing the resin in a solution containing free ^{18}F ions, following the indirect activation method described by Windows-Yule et al. [29] and Parker et al. [41].

A modified ADAC Forte camera [42] was used to track the movement of the radioactive tracer particle within the Eirich mixer. The mixer was positioned between the camera's two detectors, with the mixing pan centred, while the detectors were adjusted to be as close as possible to enhance data collection [36]. The ADAC camera can locate a tracer travelling at 1 m/s approximately 250 times a second to within 0.5 mm. This spatial accuracy can increase further to within 100 μm for slower tracers. Additional details on the ADAC camera can be found in Parker et al. [43] and Herald et al. [42]. Annihilation of the β^+ particles very close to the tracer particle produces back-to-back gamma rays which are detected by the camera. Triangulation of these events using the PEPT-ML algorithm enables the tracer position to be obtained in three dimensions in Cartesian co-ordinates and time (x, y, z, t). This algorithm has the capability to further improve precision and confidence in tracer position by using a machine learning clustering algorithm [44] and has been applied previously for the wet blending of electrode materials [45] due to its excellent balance of temporal and spatial resolution [29]. Particle trajectories and velocities were also calculated using PEPT-ML and then a Eulerian grid was applied using the UP4 (Universal Post Processor for Particulate Processes) toolset to allow for the generation of number fields and velocity fields as well as 3D free surface plots [46].

2.3. PEPT data filtering methodology

To compare the PEPT and DEM results on a valid basis, it is necessary to have high statistical confidence in the tracer occupancy and the resulting velocities calculated from the PEPT data. This requires a sufficient number of tracer detections in each voxel of the mixer internals once the data is discretised onto a Eulerian grid. This may be interrogated using the particle occupancy, defined as the fraction of the total time that the particle spends within a given location in the vessel [36,47]. As can be seen in Fig. 2(a) there are low occupancy regions predominantly in the centre of the vessel. Areas of low occupancy are thus filtered out by removal of any grid points where the occupancy is below one standard deviation from the average over all grid points, shown in Fig. 2(b). One standard deviation was chosen due to the wide distribution of occupancy throughout the vessel, as can be seen in the histogram of occupancy values shown in Fig. 2(c), with the histogram after filtering being shown in 2(d).

This approach provides a consistent way of improving the statistics of the PEPT data for comparison to the DEM, avoiding use of arbitrary threshold criteria which might cause large variations in filtering between datasets.

2.4. Péclet number

The Péclet number is the ratio between advective transport and diffusive transport (dispersion). From PEPT data, a Mean Squared Displacement (Eq. (1)) field can be calculated across the vessel volume, a measure of advective motion.

$$\mathrm{MSD}(\Delta t) = \left\langle \|\mathbf{r}(t+\Delta t) - \mathbf{r}(t)\|^2 \right\rangle \quad (1)$$

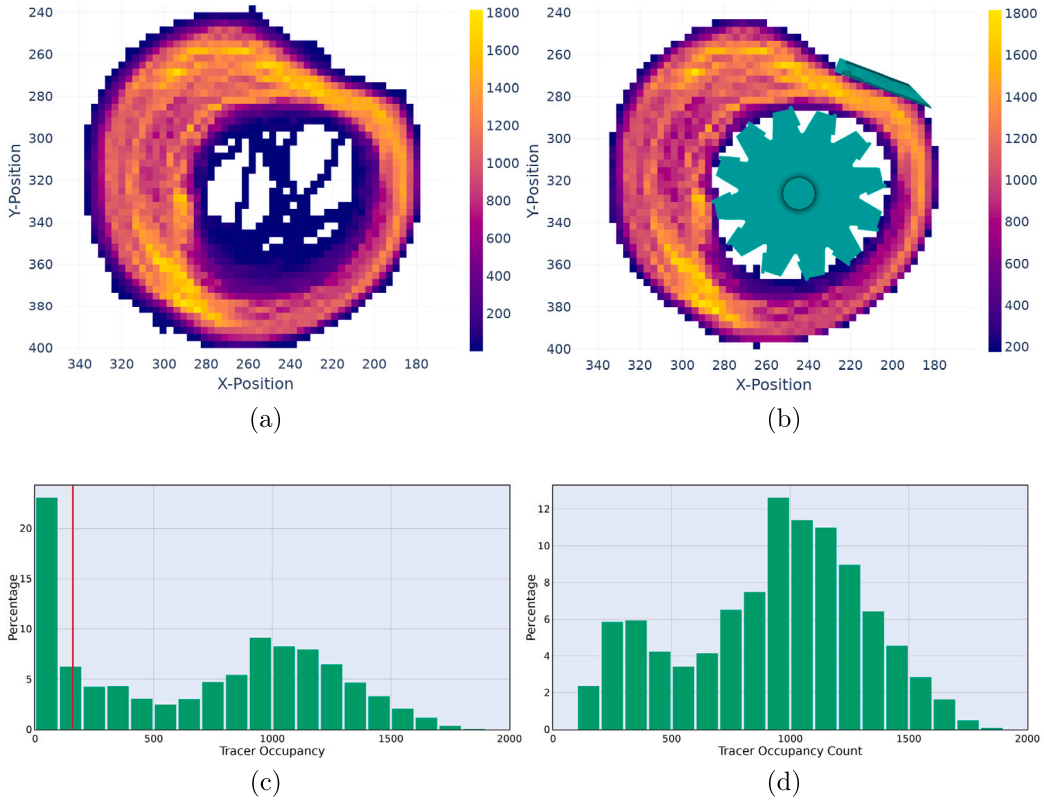

Fig. 2. Raw PEPT number field (a), PEPT number field after filtering (b), with both heat maps have x and y axis corresponding to the position within the ADAC camera. Raw PEPT data occupancy histogram (c) where the red line shows where the filtering limit is, and the resulting PEPT data occupancy histogram after filtering (d).

Table 1
Average mixer Péclet number.

Tip-speed	Average Péclet number
10 m/s	14 959
20 m/s	2067
30 m/s	2440

where $\mathbf{r}(t)$ is the position vector of a particle at time t, Δt is the time step between two observations. As previously reported [45,48], dispersion (Eq. (2)) can also be calculated from PEPT data across the vessel volume.

$$\sigma^2 = \frac{1}{n}\sum_{i=1}^{n}(x_i - \bar{x})^2 + (y_i - \bar{y})^2 + (z_i - \bar{z})^2, \tag{2}$$

where σ is the standard deviation, $\bar{x}, \bar{y}, \bar{z}$ the mean final location, and n the number of traces. Both MSD and dispersion are calculated for a 700 ms time-step, which is approximately the slowest time for a complete circulation of the PEPT tracer in the Eirich mixer, as well as a short enough time-step that dispersion is not constrained by the mixer volume. The resulting Péclet number field for 20 m/s tip-speed is shown in Fig. 3, this variation in Péclet number is also seen at 10 and 30 m/s tip-speed. For all regions of the mixer, advection dominates by several orders of magnitude, however dispersion is higher near the rotor, leading to lower values of Péclet number in the narrow region between the rotor and the pan wall. The average Péclet number for all tip-speeds is shown in Table 1.

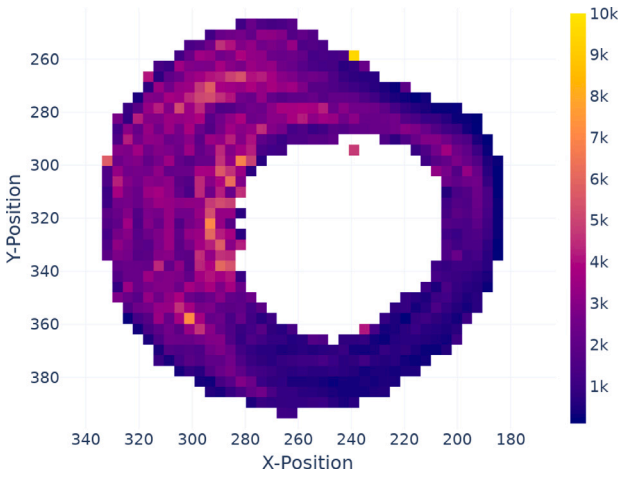

Fig. 3. Depth-averaged Péclet number for 20 m/s tip-speed PEPT data.

3. DEM simulations

The Discrete Element Method (DEM), first introduced by Cundall and Strack in 1979 [49] has been widely adopted to model dense particulate flows in myriad applications. Table 2 gives examples of DEM studies and their main findings on four commonly used mixer types (helical ribbon, paddle blender, blade and ploughshare) in literature. For all these studies the mixing tool velocities are considerably below the tool speeds investigated in this study for the Eirich EL1 mixer.

Of particular relevance to this study, DEM was previously used to analyse an Eirich R02 intensive mixer by Moreno-Juez [75] and Tokoro [76], though experimental validation of the findings was not attempted. Using DEM, the velocity of a spherical particle is set by Newton's equations of motion where all forces acting on it are in

Table 2
Literature review on DEM simulations for different mixer types.
Mixer types are: a - *helical ribbon*, b - *paddle blender*, c - *blade mixer*, d - *ploughshare*.

Author	Type	Tool speed	Main findings
Herman [50]	a	0.1–1.7 m/s	Scale-up reduces mixing efficiency and increases mixing time.
Chandratilleke [51]	a	0.3 m/s	Mixing quality depends on fill level, particle properties and tool design.
Halidan [52]	a	0.2–2.1 m/s	Impeller speed, fill level and tool design influence mixing performance.
Jin [53,54]	a	0.5–2.1 m/s	Liquid addition improves mixing performance.
Tsugeno [55]	a	0.2–0.5 m/s	Convection dominant mixing mechanism.
Gao [56]	a	0.2–1 m/s	Optimal mixing performance depends on tool speed.
Golshan [57]	a	0.5–1 m/s	Mixing quality enhanced by tool speed and filling method.
Kaneko [58]	a	0.3–0.6 m/s	Mixing performance critically influenced by bed height.
Qian [59]	a	0.2–1 m/s	Combining anchor and ribbon design enhances mixing efficiency.
Wang [60]	a	0.1–0.4 m/s	Scale-up depending on tool design and speed.
Jadidi [61]	b	0.25–0.4 m/s	Paddle geometry influences mixing time and homogeneity.
Hassanpour [62]	b	0.3–1.9 m/s	Good agreement between DEM and PEPT measurements.
Ebrahimi [63]	b	0.5–1.1 m/s	Diffusion dominates over convection in bi-disperse particle systems.
Emmerink [64]	b	0.8–3.1 m/s	Mixing quality is governed by tool speed and particle filling.
Garneoui [65]	b	0.1–0.3 m/s	Top filling and paddle number of five yields optimal mixing performance.
Wang [66]	b	0.6–0.9 m/s	Mixing is dominated by diffusion and optimal for paddle angles of 30°-45°.
Yaraghi [67]	b	0.1–0.8 m/s	Mixing quality is influenced by impeller speed.
Boonkanokwong [68]	c	0.05–1 m/s	Tool design, fill height and particle properties influence impeller torque.
Chandratilleke [51]	c	0.03–1.3 m/s	Impeller speed increases convective mixing and efficiency.
Castro [69]	c	0.2–2.4 m/s	Impeller design can enhance mixing quality or reduce energy demand.
Herman [70]	c	0.1–2.6 m/s	At constant Fr numbers similar flow patterns emerge for scale-up.
Alian [71]	d	0.9–3.4 m/s	Mixing time depends on impeller speed, fill level and particle size.
Cleary [72]	d	0.8–3.1 m/s	Non-spherical particle shapes decrease mixing rates.
Laurent [73]	d	0.1–1.8 m/s	Spherical DEM particles underestimate mixing efficiency of rice grains.
Zhu [74]	d	0.4–2.3 m/s	Optimised geometry improves homogeneity and reduces wear.

balance (Eq. (3)). Cohesive forces are generally more prominent in cases of very small particle sizes and drag forces may be considered when the solids move in a continuous phase other than a vacuum.

$$m\frac{du}{dt} = F_{gravitation} + F_{contact} + F_{drag} + F_{cohesion} + \cdots \tag{3}$$

Rotational velocity of the particles is solved by the torque balance described by Eq. (4) if all relevant torques such as rolling friction are known.

$$I\frac{d\omega}{dt} = \sum M \tag{4}$$

After all relevant forces and torques are applied, a time integration scheme is used to calculate the particles' translational velocity, updated position and angular velocity. Since dense granular systems are characterised by numerous collision events, the Hertz-Mindlin contact model is used [77,78], which separates the normal and tangential contact directions into separate spring and damping components. This model is the most appropriate model for small particles without large/inelastic deformation. Since NMC 622 particles are relatively rigid they are not expected to experience significant plastic deformation, even during high velocity impacts. For the normal direction the contact force is calculated as in Eq. (5), with Young's moduli E_1, E_2, Poisson ratios of particles ν_1, ν_2 in $E^* = \frac{E_1 \cdot E_2}{(1-\nu_1^2)\cdot E_2 + (1-\nu_2^2)\cdot E_1}$, the radii of the particles r_1, r_2 in $R^* = \frac{r_1 \cdot r_2}{r_1 + r_2}$ and the masses of the particles m_1, m_2 in $m^* = \frac{m_1 \cdot m_2}{m_1 + m_2}$. δ_n is the overlap in normal direction which allows the particles to have a smaller distance than the sum of their radii when in contact. This is done to mimic the elastic deformation of rigid spheres. Here, the parameter e is the coefficient of restitution.

$$F_{contact,normal} = \underbrace{k_n\delta_n}_{spring} \underbrace{-\gamma_n v_{rel,n}}_{damper} = \underbrace{\frac{4}{3}E^*\sqrt{R^*\delta_n}}_{k_n}\cdot\delta_n \underbrace{-2\sqrt{\frac{5}{6}}\cdot\frac{ln(e)}{\sqrt{ln^2(e)+\pi^2}}\cdot\sqrt{2E^*\cdot\sqrt{R^*\cdot\delta_n}\cdot m^*}}_{\gamma_n}\cdot v_{rel,n} \tag{5}$$

The tangential contact force $F_{contact,tangential}$ accounts for friction during contact. It is again divided into a spring and damping component and is calculated according to Eq. (6), with the tangential overlap δ_t, the relative tangential velocity $v_{rel,t}$ and equivalent shear modulus $G^* = \frac{E_1 E_2}{2(2-\nu_1)(1+\nu_1)E_2 + 2(2-\nu_2)(1+\nu_2)E_2}$.

$$F_{contact,tangential} = \underbrace{k_t\delta_t}_{spring} \underbrace{-\gamma_t v_{rel,t}}_{damper} = \underbrace{8G^*\sqrt{R^*\cdot\delta_n}}_{k_t}\cdot\delta_t \underbrace{-2\sqrt{\frac{5}{6}}\cdot\frac{ln(e)}{\sqrt{ln^2(e)+\pi^2}}\cdot\sqrt{8G^*\cdot\sqrt{R^*\cdot\delta_n}\cdot m^*}}_{\gamma_t}\cdot v_{rel,t} \tag{6}$$

Since very fine powders experience stronger cohesive and adhesive forces, relative to gravity, the model by Johnson, Kendall and Roberts (JKR) [79] is used to calculate the attractive surface force F_{JKR} as in Eq. (7), where γ is the surface energy in J/m^2 and a the contact surface area, calculated from the following non-linear expression $\delta_n = \frac{a^2}{R^*} - \sqrt{\frac{4\pi\gamma a}{E^*}}$. An analytical solution solving for a can be found in the work by Parteli [80].

$$F_{JKR} = \frac{4E^*a^3}{3R^*} - \sqrt{16\pi E^* a^3} \tag{7}$$

For the numerical integration of Eqs. (3) and (4) a suitable time step has to be chosen. The highest frequency that needs to be resolved stems from the highest wavelengths that can be propagated through a particle and is calculated according to Eq. (8) formulated by Rayleigh. To allow for a buffer in the calculation $\Delta t \approx 0.2 \cdot \Delta t_{Rayleigh}$ was chosen as the effective time step size for all simulations.

$$\Delta t_{Rayleigh} = \frac{\pi r_p\sqrt{\frac{\rho_p}{G}}}{0,1631\nu + 0,8766} \tag{8}$$

For real NMC 622 particles of 10 μ m diameter, the necessary time step size is $\Delta t \approx 5 \cdot 10^{-9}$ s. For a filling weight of 0.7 kg NMC 622 in an EL1 mixer, the particle number is estimated as $n_p \approx 7 \cdot 10^{11}$, which in combination with the calculated time step size leads to an extreme computational burden.

To overcome this hurdle *coarse-graining* is an established method [39,81–84], where multiple particles are tracked by one representative DEM particle. For this study a fixed value of 200 is used as a coarse-graining factor. In order to accurately predict the flow behaviour with coarse graining and to estimate the material parameters that are needed for contact modelling, different calibration experiments were used. To

Table 3
DEM parameters used for NMC 622.

Parameter	Value
particle diameter d_p	2 mm
bulk density ρ_p	2500 kg/m^3
shear modulus G	1×10^8 Pa
Poisson's ratio ν	0.25
coefficient of restitution e_{pp}	0.5
coefficient of restitution e_{pw}	0.5
coefficient of stat. friction $\mu_{s,pp}$	0.9
coefficient of roll. friction $\mu_{r,pp}$	0.075
coefficient of stat. friction $\mu_{s,pw}$	0.9
coefficient of roll. friction $\mu_{r,pw}$	0.075
surface energy γ_{pp}	0.25 J/m^2
surface energy γ_{pw}	0.04 J/m^2
number of particles n_p	46 000
coarse graining factor CGF	200

ensure a comparable particle behaviour DEM parameters have been carefully calibrated against real world experiments such as static angle of repose tests, dynamic angle of repose tests using a Schulze shear cell and rotating cylinder, as well as inclined plate test against stainless steel. These experiments were chosen to guarantee that the powder movement can be accurately simulated while maintaining reasonable calculation times. These calibration experiments can be found in [85] and the relevant simulation parameters are given in Table 3.

To estimate the influence of air movement on the particle motion, the Stokes number is calculated for a NMC 622 particle with a diameter, $d_p = 10$ µm, solids density, $\rho_p = 4650$ kg/m^3, air viscosity, $\mu_f = 1,8 \cdot 10^{-5}$ kg/ms and the distance between mixing tool and wall scraper, $L = 0.04$ m. For the air velocity field a Computational Fluid Dynamics (CFD) simulation of pure air flow in the EL1 mixer was done for the three investigated mixing tool speeds of 10 m/s, 20 m/s and 30 m/s which gave averaged air velocities between the mixing tool and the wall scraper of approximately 0.9 m/s, 1.2 m/s and 2 m/s respectively. Using these values, the Stokes number can be calculated according to Eq. (9) which indicates that the particles follow the air flow at all mixing tool speeds.

$$St = \frac{\rho_p \cdot d_p^2 \cdot u_f}{18 \cdot \mu_f \cdot L} \lessapprox 0.1 \tag{9}$$

To account for the air movement in the mixing vessel the CFD simulated velocity field is introduced into the DEM simulation to give the relative velocities v_{rel}. With this the drag force acting on the particles can be considered according to Eq. (10).

$$F_D = \frac{1}{2}\rho_f v_{rel}^2 c_D \pi r^2 \tag{10}$$

The Morsi-Alexander Drag model is used to calculate the drag coefficient C_D of spherical particles in a wide range of Reynolds numbers. The exact equations can be found elsewhere [86]. The DEM simulations were run until a quasi-static flow field was established which was usually achieved within 20 to 30 s of simulated mixing time. The proprietary software EDEM 2023 (Altair Engineering Inc, USA) was used to generate the DEM simulations.

4. Results and discussion

4.1. Comparison of PEPT and DEM velocity fields

To provide a qualitative spatial comparison between the simulations and experimental datasets, 2-D depth averaged heat maps of both the PEPT and DEM velocity fields were generated as shown in Fig. 4. Parity plots comparing the filtered PEPT velocity magnitudes to the DEM values were also developed.

Fig. 4 shows velocity fields for the DEM simulations (a), and velocity fields extracted from the raw PEPT experimental data (b), and filtered PEPT data, which illustrate the wide range of velocities in the mixer volume. The PEPT velocities were calculated using seven interpolated tracer locations from the PEPT data file which stores particle position (x, y, z) as a function of time. This value was selected to be as small as possible to allow for the detection of high velocity trajectories near to the rotor, without excessively smoothing the data. The sensitivity of the velocity distribution to this parameter was checked, with only a slight shift in the overall distribution observed. This gives rise to maximum tracer velocities which match with the tip-speed of the rotor. These maximum velocity events are rare since the tracer must be hit by the rotor with sufficient contact time to accelerate close to the rotor tip speed before being slowed by the NMC material in the vessel.

The DEM data shown in Fig. 4(a) has a high velocity region forming a small ring around the rotor, in the narrow area between the rotor and wall, before the flow comes into contact with the wall-scraper which then leads to a low velocity region around position (270,300). In the immediacy of the wall, away from the scraper, there appears to be a constant flow velocity at around 0.7 m/s, presumably as the wall pushes particles along at the pan rotation velocity (0.7 m/s) showing the benefit of co-current running of the Eirich mixer.

Fig. 4(c) shows the raw PEPT data, which includes the low occupancy regions around/under the rotor (Fig. 2(a) shows the 20 m/s example) as well as the gap between the wall and scraper. However, by filtering the PEPT data Fig. 4(b) is generated. As can be seen, the velocities in the main volume of the mixer remain unchanged; only data with poor statistical robustness is removed. Although the overall velocity field is qualitatively similar to that obtained from the DEM, the PEPT velocities in the vicinity of rotor are lower. This can be attributed to the time-averaged nature of the PEPT velocity calculations making it less likely to capture the very highest velocities that are present in the instantaneous DEM velocities. Despite this slight depression of maximum velocity, there still remains a large region of higher velocity in the narrow gap between the rotor and wall, with the same general trend as the flow comes into contact with the wall-scraper, leading to a region of lower velocity around (280,300). However, the regions of higher velocity in the PEPT are larger than that of the DEM. Fig. 4(d) shows all comparable data for 10 m/s tip-speed as a parity plot, where the higher instantaneous velocities in the DEM lead to apparent outliers above parity (red dashed line). This is expected, as is the apparent upper limit in the PEPT velocities shown in the inset at around 0.75 m/s, due to the time taken to calculate PEPT tracer velocity, as well as the depth-averaged nature of the grid. However, both parity plots show the vast majority of points lying on or near parity, providing a strong indication that the DEM model has correctly captured the physics of the system.

It is interesting to note the majority of both the DEM and PEPT velocities are below 1 m/s, whilst the rotor tip-speed is 10 m/s, showing that momentum transport is much lower for dry mixing in the Eirich when compared to wet mixing, where similar PEPT tracer velocities were seen at tip-speeds as low as 2 m/s [45]. Furthermore, the heterogeneous nature of material movement means that it is key to establish good vessel turnover, to ensure that all material has the opportunity to be exchanged through all the different regions of the mixer to yield a homogeneously mixed product.

For 20 m/s tip-speed, good qualitative agreement between the DEM and PEPT datasets is again observed, as shown in Fig. 5. The DEM data shown in Fig. 5(a) still has a ring of highest velocities in the narrow region between the rotor and wall (bottom right), with the central region of the vessel (280,300) having the lowest velocity. However, the velocities in the region where the flow is disrupted by the wall-scraper (240,280) are slightly higher for PEPT than the DEM and the high velocity region is slightly larger. The impact on filtering the PEPT data is much clearer with the 20 m/s dataset, with Fig. 5(c) showing the occasional trajectories at high velocity when the PEPT tracer passes through the region occupied by the rotor, which are then not present in Fig. 2(b). The velocities in the main volume of the material are again not impacted by the filtering process. Comparison between the DEM

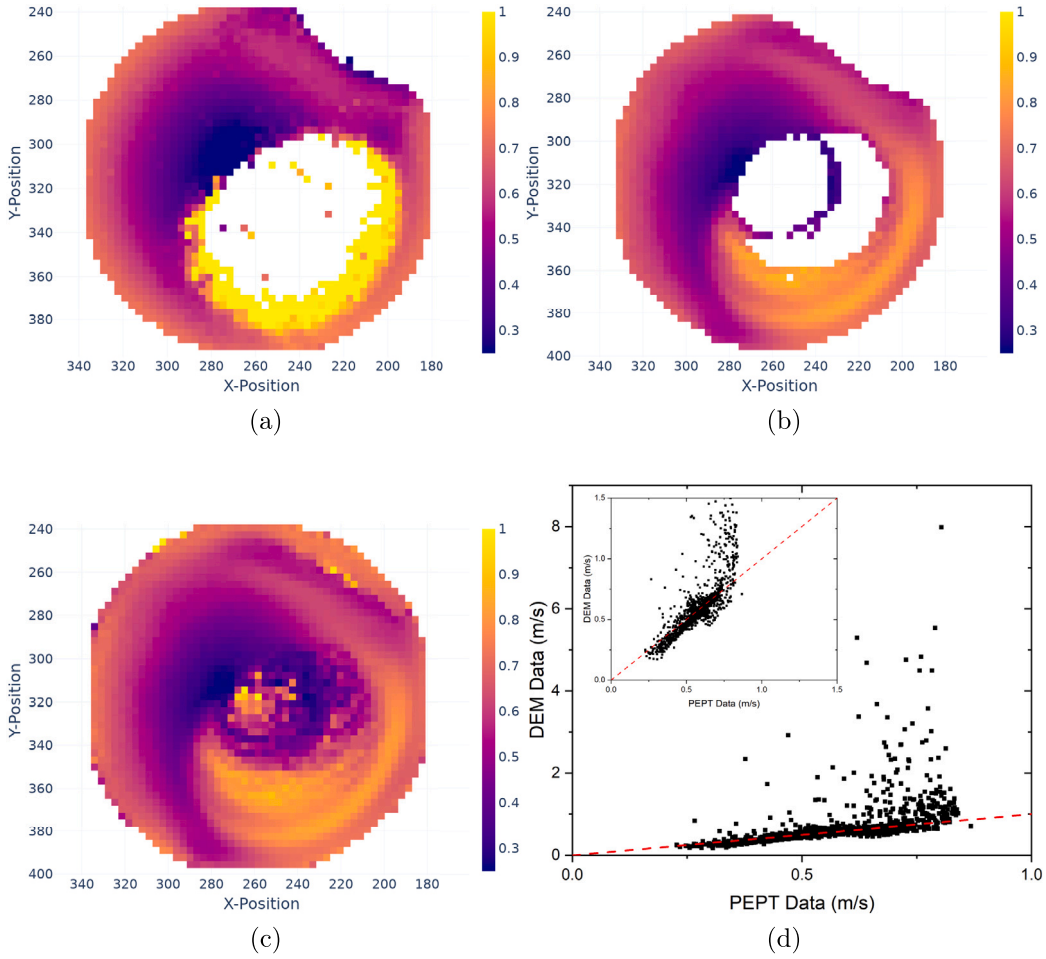

Fig. 4. DEM velocity field (a) with filtered (b) and raw (c) PEPT data velocity field, as well as a parity plot (d) comparing the DEM and filtered PEPT velocities. For 10 m/s tip-speed.

5(a) and PEPT 5(b) shows the same trends present in both, with the highest velocity in both being located around (260,370). This is due to the high velocity tracer trajectories seen in Fig. 5(c), where the tracer is ejected from the material flow, passes through the rotor region at high velocity and then rejoins the material at higher velocity than if it had followed the general material flow. The velocities close to the vessel wall are similar in both experiments and simulation, as was the case for a rotor tip speed of 10 m/s. The parity plot shown in Fig. 5(d) shows how there continues to be reasonable agreement at lower velocities, with the majority of the outliers explainable due to the high DEM velocity for some grid zones as seen at 10 m/s.

At 30 m/s tip-speed, the same general features are observable. The high velocity region at the bottom right is larger than at lower tip-speeds, reaching almost to the wall. The velocity gradient around the wall-scraper is again present, with the particles having the lowest velocity again around (280,300). For the PEPT data 6(c), the filtering has a larger impact due to the high number of trajectories passing through the centre over/under the rotor. The filtered PEPT data 6(b) does show the same slow moving area, with minimum velocities (280,300) as the DEM and other PEPT datasets at lower tip speeds, but does have a smaller region around (290,330). The reason is unclear, but may be a consequence of poorer statistics close to the rotor due to a much larger data removal in filtering. This is seen in the parity plot 6(d) where the distribution of points is compacted on the x axis due to the narrower range of velocities present in the PEPT data.

Table 4 shows the median, mean and standard deviation of velocities for each dataset. These are calculated from the raw velocities. At all tip-speeds, the median for both the PEPT and DEM datasets are almost identical, and the mean values agree reasonably well, with the largest difference being at 30 m/s tip-speed where the PEPT data mean is 0.059 m/s (8.4%) higher than the DEM mean. This can be attributed to the higher minimum velocities observed in the PEPT data, shown in Fig. 6(b). The 30 m/s dataset also has the largest number of trajectories in the rotor region, however, these are likely to have a smaller impact on the mean velocity as the DEM also shows very high velocities as seen in the parity plot in Fig. 6(d) .

Table 4
Summary of key statistics for PEPT experiment velocities, and DEM simulation velocities, all units are m/s.

Dataset	Median	Mean	St. Dev.
PEPT - 10 m/s	0.590	0.599	0.204
DEM - 10 m/s	0.595	0.614	0.319
PEPT - 20 m/s	0.637	0.681	0.289
DEM - 20 m/s	0.636	0.659	0.388
PEPT - 30 m/s	0.670	0.762	0.362
DEM - 30 m/s	0.670	0.703	0.464

Overall, there is reasonable agreement between the DEM and PEPT data in Figs. 4–6, with all datasets showing the same key features: a high velocity region in the narrow gap between the rotor and wall (bottom right all heat maps), flow disrupted by the wall-scraper (top right) which leads to a lower velocity around the wall-scraper, followed by a lower velocity region in the central portion of vessel around

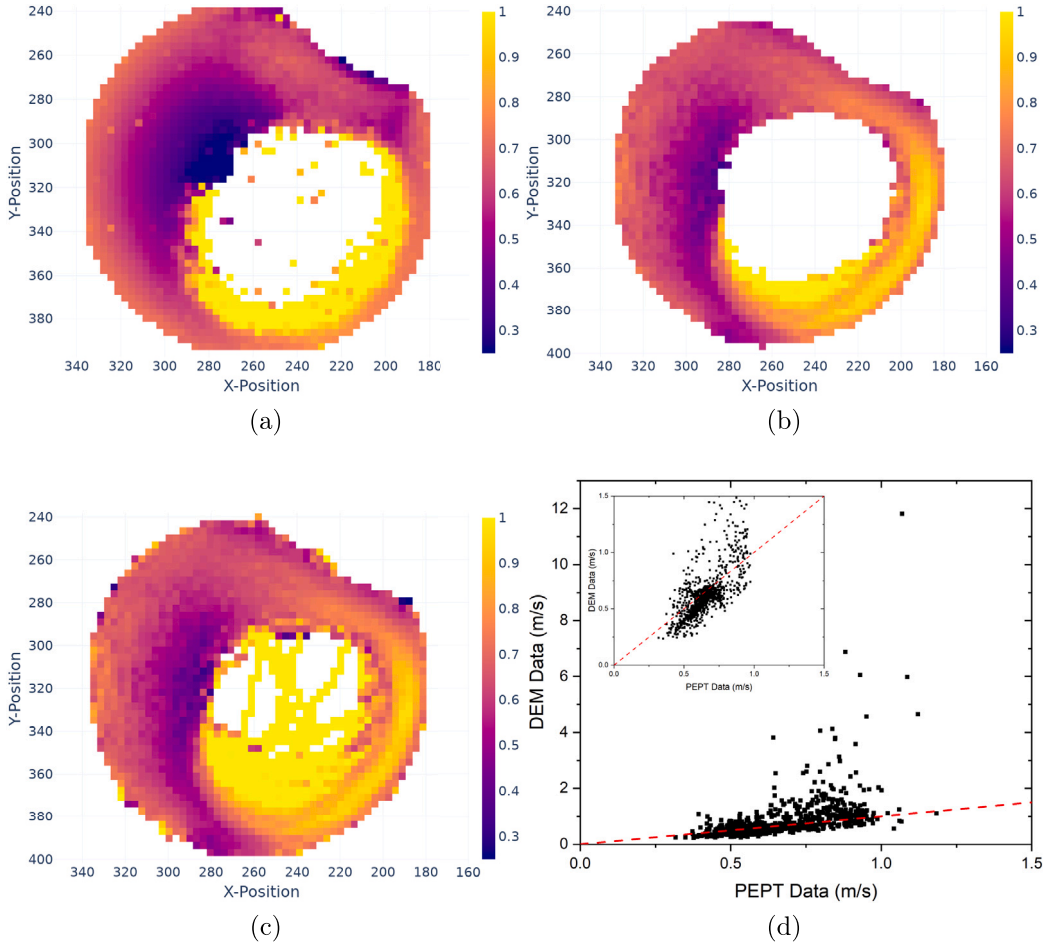

Fig. 5. DEM velocity field (a) with filtered (b) and raw (c) PEPT data velocity field, as well as a parity plot (d) comparing the DEM and filtered PEPT velocities. For 20 m/s tip-speed.

(280,300). The high velocity region increases with tip-speed for both the DEM and PEPT, and the velocity of the low region is similar for all DEM simulations but does appear to increase with tip-speed in the PEPT experiments.

4.2. Identification of material free surface in PEPT and DEM

Comparison of the free-surface dynamics between the PEPT and DEM data provides another means through which to assess the accuracy of the simulations. The location of the free surface changing with tip speed has previously been seen in a wet anode slurry mix in the Eirich mixer [45].

Fig. 7 shows the free surfaces for the PEPT (left) and DEM (right) datasets, with the PEPT data being a surface plot of tracer occupancy, and the DEM showing a snapshot of the particle positions. Under the assumption of ergodicity, it is reasonable to take these surfaces as equivalent [47]. The PEPT surface is thresholded to remove the bottom 5% of occupancy counts. This removes the individual trajectories that can occur in and around the rotor (such as those seen in Fig. 2(a)). Both the PEPT and DEM show excellent agreement at 10 m/s tip-speed, with a similar region where the free surface detaches from the rotor towards the wall scraper.

At 20 m/s tip-speed, as shown in Fig. 8 both the PEPT and the DEM show that the granular material becomes further disengaged from the rotor, leaving more pins of the rotor not in contact with the material, which provides a possible explanation as to why there is a larger region of low velocity in Fig. 5. This trend continues at 30 m/s, shown in Fig. 9, with an even smaller edge of the free surface of the granular material being in contact with the blades of the rotor (highlighted in Fig. 10). This pulling away of the free surface from the rotor is key when considering the performance of the mixer at higher tip-speeds, as will be discussed further in the next section. Whilst this behaviour is unlike previous PEPT experimental data studying anode mixing, the density of NMC 622 is significantly higher, and the dry nature of the mixing would lead to less energy transport throughout the material, causing the material to be thrown less up the side of the mixer and to sink back down quicker when compared to a wet slurry or fluid.

4.3. Granular temperature and free surface changes

Granular temperature is used to describe the random motion and kinetic energy of particles in a granular material, analogous to thermal temperature in molecular systems [87]. The granular temperatures presented are calculated in EDEM Altair using Eq. (11), where t_g is the granular temperature, $v_i(t)$ is the velocity of particle i at time t, and $v(r_i(t), t)$ is the velocity of the particle at position $r_i(t)$ and time t.

$$tg = \frac{1}{3}\left\langle \sum_i \left(v_i(t) - v(r_i(t), t)\right)^2 \right\rangle \tag{11}$$

Figs. 11 and 12 show granular temperature along the 2 planes shown in Fig. 1(a), one in line with the paddle element of the rotor, and one in line with the downwards facing pins at the bottom of the rotor. For both planes, the granular temperature are qualitatively similar and

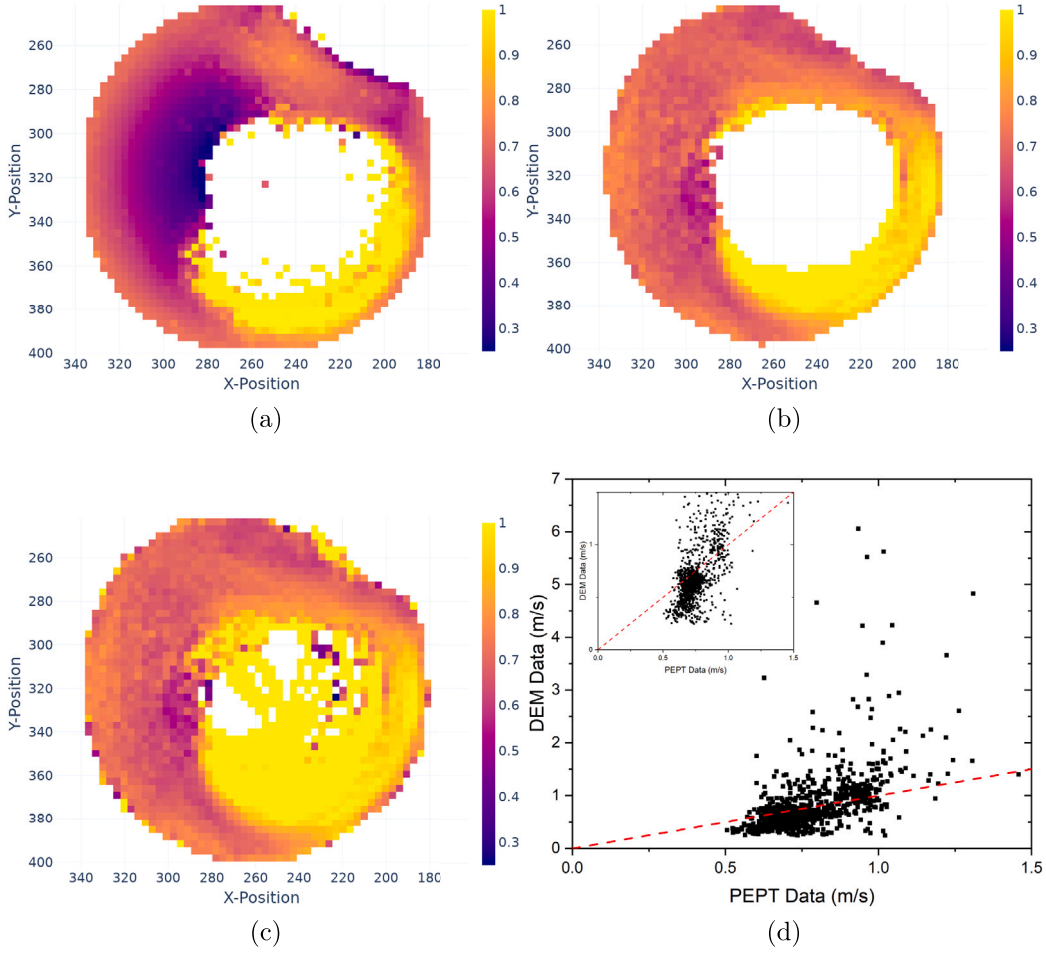

Fig. 6. DEM velocity field (a) with filtered (b) and raw (c) PEPT data velocity field, as well as a parity plot (d) comparing the DEM and filtered PEPT velocities. For 30 m/s tip-speed.

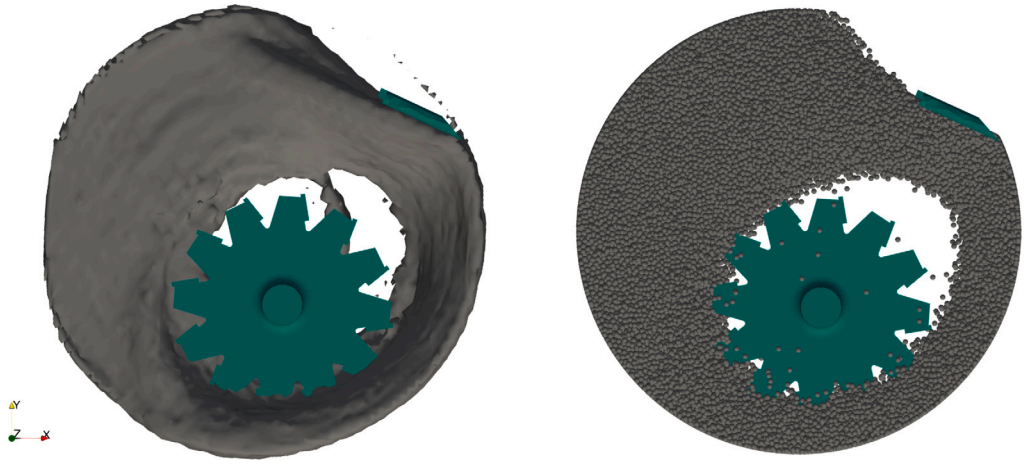

Fig. 7. Free surface of PEPT (left) and DEM (right) data at 10 m/s tip-speed.

do not change significantly with increasing tip-speed, with all having the highest granular temperature in the region immediately around the rotor, and a lower but larger area region at the edge of the wall-scraper (top right of each heatmap). In the region around the rotor, the area of high granular temperature is observed to increase slightly with tip speed, but the magnitude of change is much less than the concomitant increase in tip-speed.

Figs. 11(d) and 12(d) show the dependence of granular temperature for each tip-speed upon simulation time. For both planes and all tip-speeds the length of simulation has little to no impact on the granular temperatures calculated.

The relative insensitivity of the granular temperature in the bulk flow to the changes in rotor tip speed confirms the poor momentum transport through the dry powder due to the limited region of high

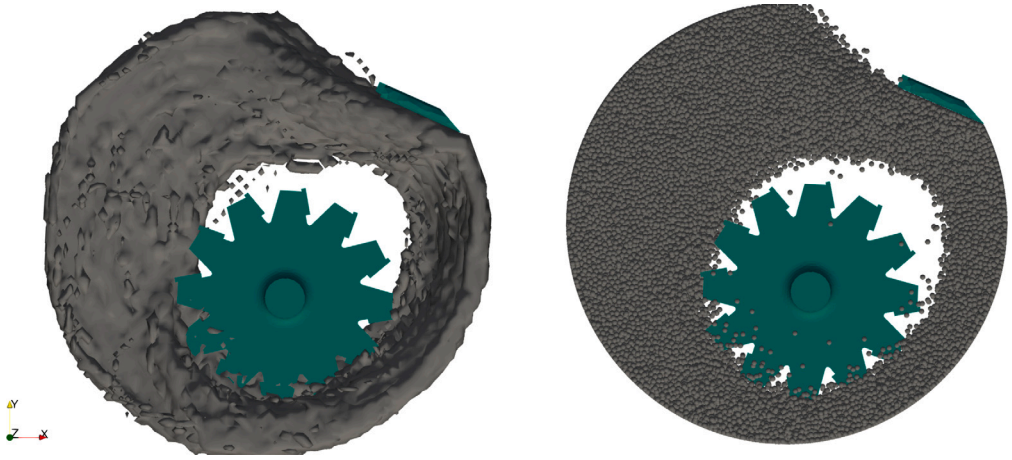

Fig. 8. Free surface of PEPT (left) and DEM (right) data at 20 m/s tip-speed.

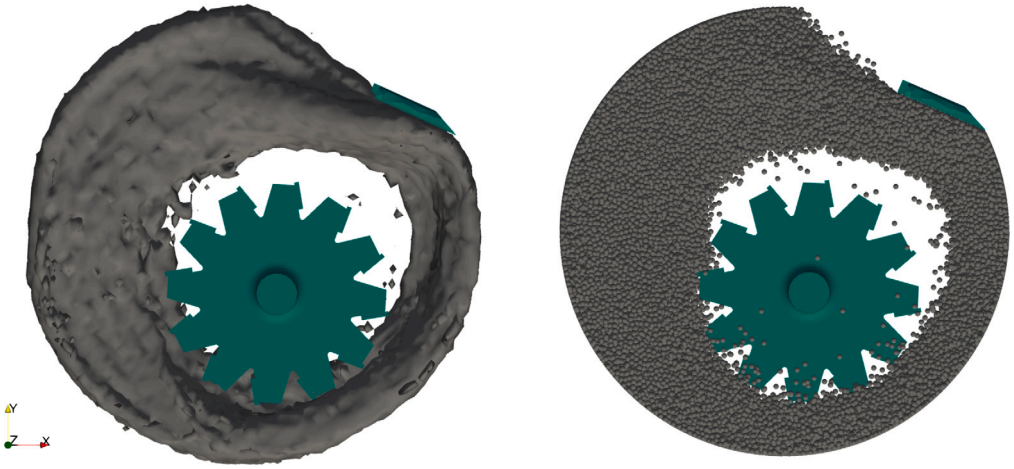

Fig. 9. Free surface of PEPT (left) and DEM (right) data at 30 m/s tip-speed.

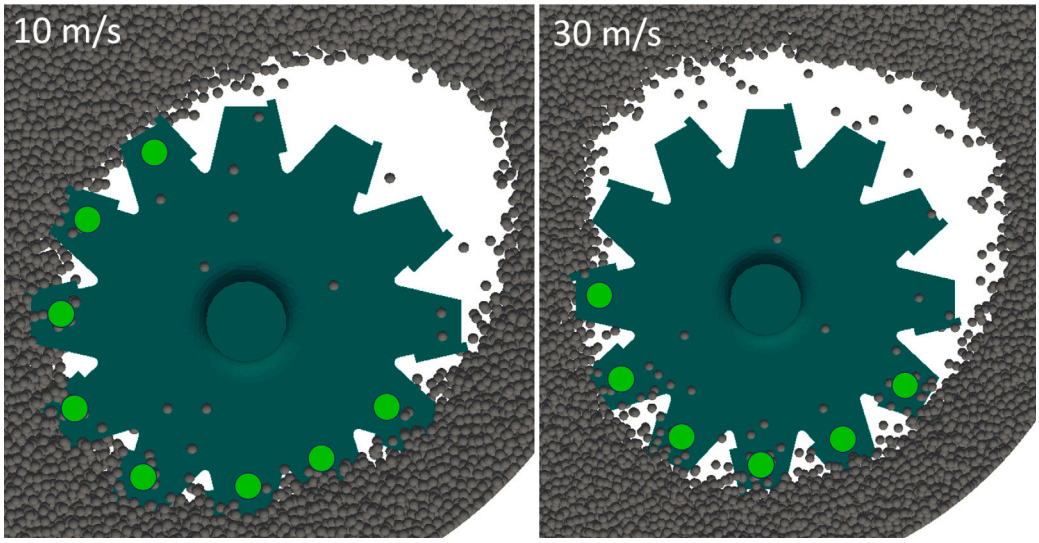

Fig. 10. Zoomed in view of the rotor and free surface at 10 m/s and 30 m/s tip-speed.

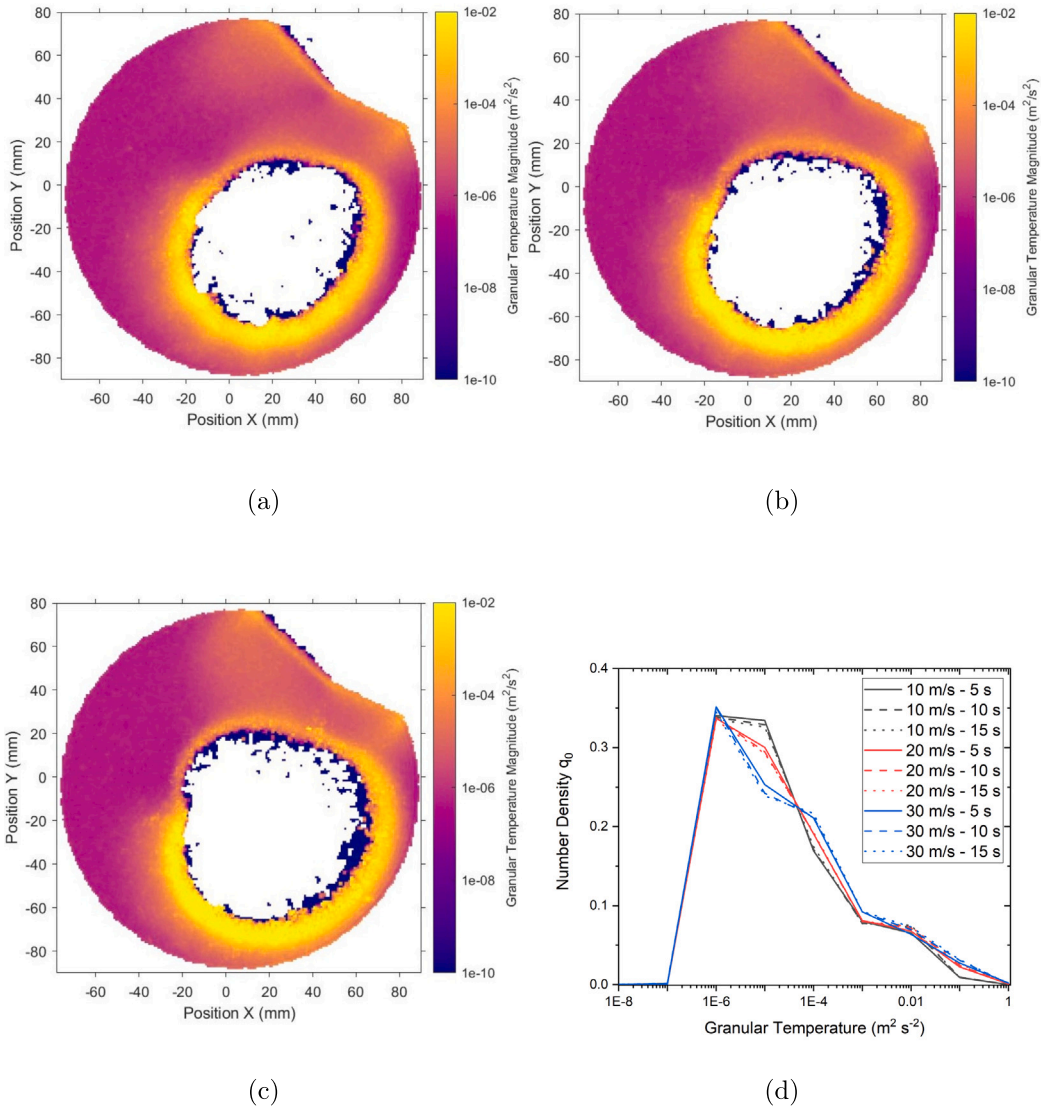

Fig. 11. DEM granular temperature field for 10 m/s (a) 20 m/s (b) and 30 m/s (c) tool speed at plane height of 1 mm above vessel bottom (plane 1 in Fig. 1(a)). Number density plots for granular temperature (d) comparing different tip speeds and averaging intervals between 5 s and 15 s simulation time.

temperature around the rotor, and also shows the importance of the other elements of the mixer (rotating pan and wall-scraper) in generating mixing. Furthermore, as the free surface pulls away from the rotor, the granular temperature at the edge of the material is similar, even if it is further away from the rotor.

Fig. 13 shows depth-averaged granular temperature fields close to the rotor at 10 and 30 m/s tip-speed. They both show a region of higher granular temperature immediately around the rotor, this confirms the presence of a granular gas as seen in Fig. 10, with particles being free of the surrounding granular fluid. This can also be seen in the unfiltered PEPT data shown in Fig. 6(c) where the PEPT tracer leaves the material and passes through void region.

The granular temperature of this region increases with tip-speed, leading to outward pressure from the increased energy input. This "bubble" of granular gas then expands due to the higher granular temperature into the least constrained region of the vessel, which is the side of the rotor furthest from the pan wall, resulting in the free surface disengagement observed in both the PEPT data and DEM simulations.

4.4. Estimation of transient mixing time from DEM

As the free surface of the granular material disengages from the rotor, there is a potential outcome that higher tip-speeds will give diminishing returns in terms of mixing performance. Given the above discussion, where the DEM simulations have been shown to provide a reasonable approximation of the physical system, they have been used to evaluate the transient mixing behaviour, which is challenging to reproduce from PEPT data. The Lacey mixing index [88] for each tip-speed was calculated by splitting the DEM particles into 2 groups (x-axis split is shown in Fig. 15(a) and the 3 axis along which particles were separated in Fig. 14(b)) which are completely segregated at first, and then calculating how they become mixed over time. The optimal number of bins was determined through a mesh-independence study where radial, azimuthal, and vertical splits were systematically varied whilst monitoring changes in the Lacey mixing index. The analysis showed that increasing beyond 6 radial, 8 azimuthal, and 30 vertical divisions produced negligible improvements, and this configuration

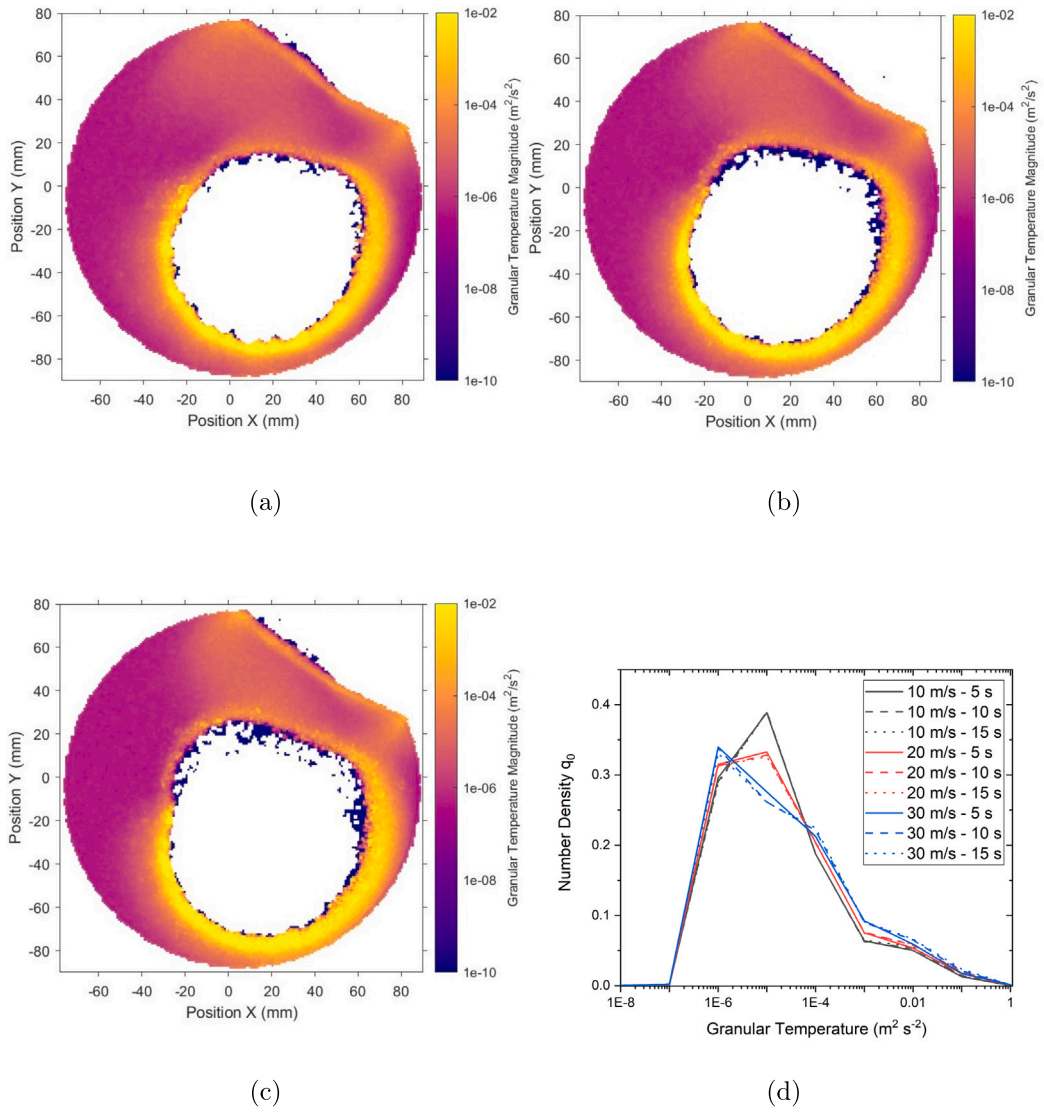

Fig. 12. DEM granular temperature field for 10 m/s (a) 20 m/s (b) and 30 m/s (c) tool speed at plane height of 8 mm above vessel bottom (plane 2 in Fig. 1(a)). Number density plots for granular temperature (d) comparing different tip speeds and averaging intervals between 5 s and 15 s simulation time.

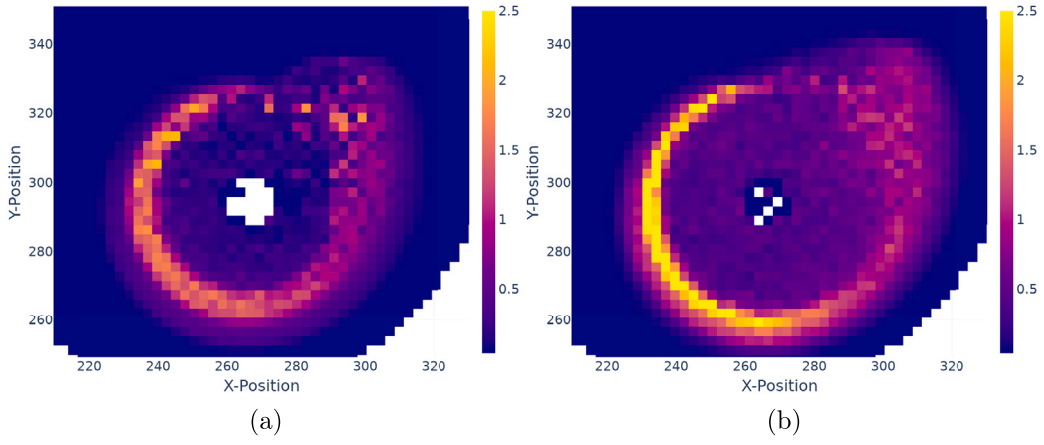

Fig. 13. Granular temperature calculated for the granular gas region for 10 (a) and 30 (b) m/s tip-speed.

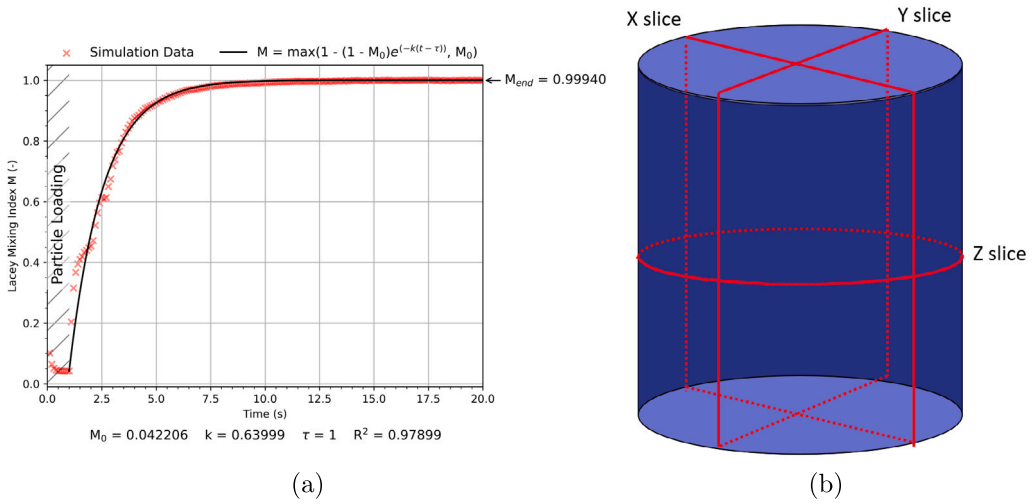

Fig. 14. X-axis Lacey mixing index calculated from the DEM simulation at 30 m/s tip-speed (a), and diagram showing each axis that particles were divided along for x, *y* and z axes.

was therefore selected. Three snapshots of this can be seen in Fig. 15, with each group separated before mixing 15(a), during the mixing where the 2 groups are partially-mixed 15(b), and when both groups have reached a mixed steady-state 15(c).

As the tip-speed increases, the mixing rates for*x* and *y* direction both increase, as shown in Figs. 15(d) and 15(e), which is quantified by value k from the fit equation shown in Fig. 14(a) and Eq. (12).

$$M = \max\left(1 - (1 - M_0)e^{-k(t-\tau)},\ M_0\right) \tag{12}$$

The k values for the x and y directions for each tip-speed are similar to one another as would be expected, 0.454 and 0.463 for 10 m/s, 0.566 and 0.591 for 20 m/s, and 0.640 and 0.667 for 30 m/s respectively. Despite the larger variation for 20 and 30 m/s when compared to 10 m/s, this is markedly smaller when compared to the change between tip-speeds. However, tip-speed does not appear to impact mixing in the z-axis, as seen in Fig. 15(f). This difference can be rationalised by the fact that the height of the free surface is not impacted by tip-speed, and if there was a change in mixing rate in the z direction, it would be expected that material would be centrifuged higher up the vessel sides and thus impact the height of the free surface. Despite the x and y directions requiring much more movement to become fully mixed when compared to the relatively low fill height for the z direction, the fact that solid body rotation is the main driving force behind the mixing in the Eirich mixer leads to similar Lacey times for the x, y and z directions. In all directions, there is little to no impact on mixing time with increased tip-speed, showing the significantly diminishing returns due to the free surface of the material disengaging from the rotor at higher tip-speeds. Assuming a constant power number, a reduction in tip-speed from 30 m/s to 10 m/s could lead to approximately a 27-fold reduction in power, with little impact on mixing time.

Whilst the Lacey mixing index between NMC 622 particles does not directly capture the dynamics of coating the NMC 622 with the carbon black nanoparticles, it provides a useful proxy measurement: the more rapid the turnover of, and intermixing between, the NMC particles, the more rapidly one may expect them to obtain an even coating of carbon black.

A heavily coated NMC 622 particle can have carbon black knocked off by either interaction with another particle or interaction with the mixer. If the NMC particle it interacted with is poorly coated, then the carbon black become more evenly distributed between the 2 particles. If the carbon black is removed from the NMC 622 particle surface by the mixer, then it is free to coat another NMC 622 particle that enters that region of the mixer. Thus high vessel turnover will improve the consistency of coating by ensuring that many particles interact with one another and all of the regions of the mixer.

The results show that each particle can be expected to experience all of the mixing regions within the vessel. The rapid and homogeneous nature of the particles' intermingling shows that larger clumps of unmixed particles are highly unlikely, and will lead to each particle interacting with many other particles within a rapid timeframe. As such, any particles highly loaded with carbon black will likely interact with many particles which are under loaded or not coated with carbon black, which will lead to a better distribution of carbon black over all particles over a mix, typically of 2 to 5 minutes' duration (*cf.* the observed mixing time of ~ 15 s).

5. Conclusions

Using the Positron Emission Particle Tracking (PEPT) technique, we have provided first experimental insight into the three-dimensional dynamics of dry powder blending within an Eirich mixer. The velocity field data obtained have been used to validate a discrete element method (DEM) model. Considering the large degree of coarse graining required for the DEM simulations, agreement between PEPT and DEM is very good, demonstrating that even this simplified model can successfully capture the fundamental dynamics of the system, though careful calibration will be necessary before extension to systems at different scales.

Both experimental and numerical results identified a large area mostly devoid of material in the centre round the rotor, a region of high velocity in the narrow channel between the rotor and pan wall, velocities decreasing as flow is disrupted by the wall-scraper, followed by a central region of the lowest velocity (but not zero movement). As tip-speed is increased, the free surface of the material appears to disengage from the rotor, believed to be caused by an increase in granular temperature of the granular gas around the rotor. This increase in granular temperature then exerts an outward pressure which causes the material to disengage in the least constrained region of the mixer.

The validated DEM data was then used to estimate the transient mixing dynamics. It was observed that while increasing the rotor tip speed increased the rate of mixing within the system, the increase was modest even when tripling the rotor speed, and showed diminishing returns. The origin of these diminishing returns is thought to be an increased tendency for the powder bed to disengage from the rotor as tip-speed increases.

Due to the commodity nature of Li-ion batteries, even small incremental optimisations of individual manufacturing steps can yield

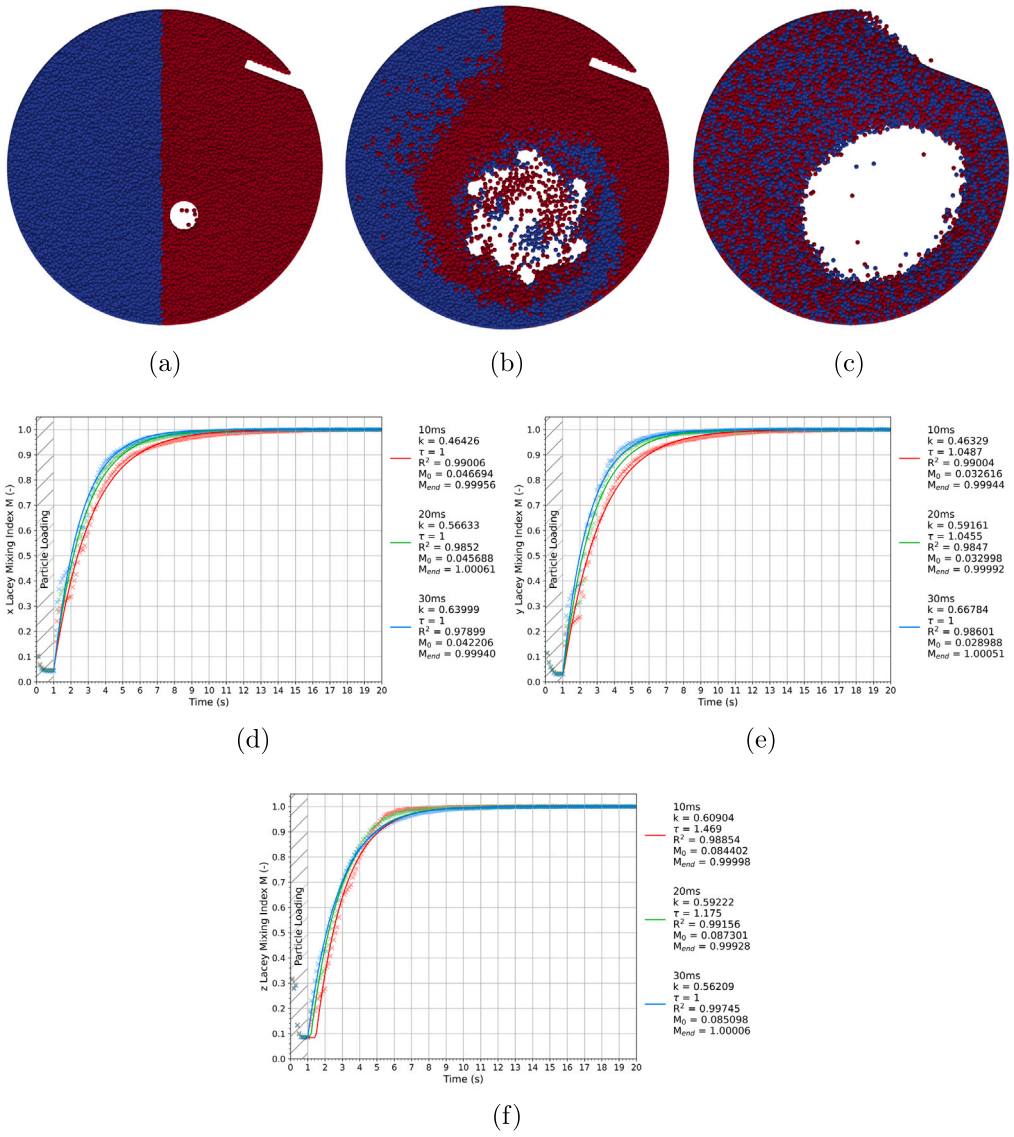

Fig. 15. DEM simulation for 10 m/s with the particles split into 2 groups, before mixing (a), during mixing (b) and when fully mixed (c). With the Lacey mixing index for all tip-speeds for the *x*-axis (d), *y*-axis (e), and *z*-axis (f).

significant improvements in sustainability both in a environmental and financial sense. With this work the diminishing returns with tip-speed show a clear avenue to reduce the energy use in the mixing process. Whilst the energy costs of mixing are modest compared to the drying step, future use of the validated DEM model allows for the exploration of mixer dynamics across a broader and denser parameter space for potentially a wider variety of electrode materials than would be feasible experimentally, with consequent advances possible in dry processing and product optimisation.

CRediT authorship contribution statement

S.D. Hare: Writing – review & editing, Writing – original draft, Visualization, Validation, Formal analysis. **C. Lischka:** Writing – review & editing, Writing – original draft, Visualization, Software, Data curation. **J. Grogan:** Visualization, Software, Methodology. **D. Werner:** Visualization, Software, Methodology. **H. Nirschl:** Writing – review & editing, Supervision, Funding acquisition. **E. Kendrick:** Writing – review & editing, Supervision, Funding acquisition. **C.R.K. Windows-Yule:** Writing – review & editing, Validation, Supervision, Resources, Methodology. **M.J.H. Simmons:** Writing – review & editing, Validation, Supervision, Resources, Methodology, Funding acquisition.

Declaration of competing interest

The authors declare the following financial interests/personal relationships which may be considered as potential competing interests: Sam Hare reports financial support was provided by The Faraday Institution. Clemens Lischka reports financial support was provided by German Federal Ministry of Education and Research (BMBF). If there are other authors, they declare that they have no known competing financial interests or personal relationships that could have appeared to influence the work reported in this paper.

Acknowledgements

Part of this work was supported by the Faraday Institution NEXTRODE project (faraday.ac.uk; EP/S003053/1, FIRG015).

Part of this work was supported by the Federal Ministry of Education and Research Germany (BMBF) for funding this work in the project Sim4Pro (grant number 03XP0242B) within the ProZell Cluster.

The PEPT computations described in this paper were performed using the University of Birmingham's BlueBEAR HPC service, which provides a High Performance Computing service to the University's

research community. See http://www.birmingham.ac.uk/bear for more details.

Data availability

Data will be made available on request.

References

[1] Julio A. Sanguesa, Vicente Torres-Sanz, Piedad Garrido, Francisco J. Martinez, Johann M. Marquez-Barja, A review on electric vehicles: Technologies and challenges, Smart Cities 4 (1) (2021) 372–404.

[2] Lere Deguenon, Daniel Yamegueu, Sani Moussa kadri, Aboubakar Gomna, Overcoming the challenges of integrating variable renewable energy to the grid: A comprehensive review of electrochemical battery storage systems, J. Power Sources 580 (2023) 233343.

[3] Laura J. Sonter, Marie C. Dade, James E.M. Watson, Rick K. Valenta, Renewable energy production will exacerbate mining threats to biodiversity, Nat. Commun. 11 (1) (2020) 4174.

[4] Isabella D.R. Stephens, Peter Slater, Emma Kendrick, A perspective on cell bill of materials using BatPaC, J. Power Sources 631 (2025) 236170.

[5] Ahmad Mayyas, Darlene Steward, Margaret Mann, The case for recycling: Overview and challenges in the material supply chain for automotive li-ion batteries, Sustain. Mater. Technol. 19 (2019) e00087.

[6] Simon Davidsson Kurland, Energy use for GWh-scale lithium-ion battery production, Environ. Res. Commun. 2 (1) (2020) 012001.

[7] Florian Degen, Marius Schütte, Life cycle assessment of the energy consumption and GHG emissions of state-of-the-art automotive battery cell production, J. Clean. Prod. 330 (2022) 129798.

[8] F. Degen, M. Winter, D. Bendig, J. Tübke, Energy consumption of current and future production of lithium-ion and post lithium-ion battery cells, Nat. Energy 8 (11) (2023) 1284–1295.

[9] Florian Degen, Lithium-ion battery cell production in Europe: Scenarios for reducing energy consumption and greenhouse gas emissions until 2030, J. Ind. Ecol. 27 (3) (2023) 964–976.

[10] Patrick S. Grant, David Greenwood, Kunal Pardikar, Rachel Smith, Thomas Entwistle, Laurence A. Middlemiss, Glen Murray, Serena A. Cussen, M.J. Lain, M.J. Capener, M. Copley, Carl D. Reynolds, Sam D. Hare, Mark J.H. Simmons, Emma Kendrick, Stanislaw P. Zankowski, Samuel Wheeler, Pengcheng Zhu, Peter R. Slater, Ye Shui Zhang, Andrew R.T. Morrison, Will Dawson, Juntao Li, Paul R. Shearing, Dan J.L. Brett, Guillaume Matthews, Ruihuan Ge, Ross Drummond, Eloise C. Tredenick, Chuan Cheng, Stephen R. Duncan, Adam M. Boyce, Mona Faraji-Niri, James Marco, Luis A. Roman-Ramirez, Charlotte Harper, Paul Blackmore, Tim Shelley, Ahmad Mohsseni, Denis J. Cumming, Roadmap on Li-ion battery manufacturing research, J. Phys. Energy 4 (4) (2022) 042006.

[11] Jia-He Kuo, Chia-Chen Li, Water-based process to the preparation of Nickel-Rich $Li(Ni_{0.8}\ Co_{0.1}\ Mn_{0.1}\ )O_2$ Cathode, J. Electrochem. Soc. 167 (10) (2020) 100504.

[12] Brandon Ludwig, Zhangfeng Zheng, Wan Shou, Yan Wang, Heng Pan, Solvent-free manufacturing of electrodes for lithium-ion batteries, Sci. Rep. 6 (1) (2016) 23150.

[13] Brandon Ludwig, Jin Liu, I-Meng Chen, Yangtao Liu, Wan Shou, Yan Wang, Heng Pan, Understanding interfacial-energy-driven dry powder mixing for solvent-free additive manufacturing of li-ion battery electrodes, Adv. Mater. Interfaces 4 (21) (2017) 1700570, _eprint: https://onlinelibrary.wiley.com/doi/pdf/10.1002/admi.201700570.

[14] Young Jin Nam, Dae Yang Oh, Sung Hoo Jung, Yoon Seok Jung, Toward practical all-solid-state lithium-ion batteries with high energy density and safety: Comparative study for electrodes fabricated by dry- and slurry-mixing processes, J. Power Sources 375 (2018) 93–101.

[15] Yoshiyuki Komoda, Kaoru Ishibashi, Kentaro Kuratani, Ruri Hidema, Hiroshi Suzuki, Hironori Kobayashi, Rheological interpretation of the structural change of LiB cathode slurry during the preparation process, JCIS Open 5 (2022) 100038.

[16] Diana Zapata Dominguez, Jiahui Xu, Yasmina Boudjema, Siwar Ben Hadj Ali, Franco M. Zanotto, Alejandro A. Franco, Influence of the mixing speed in the rheology of NMC622-based Li-ion battery electrode slurries, J. Power Sources Adv. 26 (2024) 100141.

[17] Kwang Man Kim, Woo Sung Jeon, In Jae Chung, Soon Ho Chang, Effect of mixing sequences on the electrode characteristics of lithium-ion rechargeable batteries, J. Power Sources 83 (1) (1999) 108–113.

[18] Werner Bauer, Dorit Nötzel, Valentin Wenzel, Hermann Nirschl, Influence of dry mixing and distribution of conductive additives in cathodes for lithium ion batteries, J. Power Sources 288 (2015) 359–367.

[19] Ayaka Yonaga, Shigehiro Kawauchi, Yuki Mori, Liu Xuanchen, Shota Ishikawa, Keita Nunoshita, Gen Inoue, Takuro Matsunaga, Effects of dry powder mixing on electrochemical performance of lithium-ion battery electrode using solvent-free dry forming process, J. Power Sources 581 (2023) 233466.

[20] Carl D. Reynolds, Sam D. Hare, Peter R. Slater, Mark J.H. Simmons, Emma Kendrick, Rheology and structure of lithium-ion battery electrode slurries, Energy Technol. 10 (10) (2022) 2200545, _eprint: https://onlinelibrary.wiley.com/doi/pdf/10.1002/ente.202200545.

[21] Clemens Lischka, Stefan Gerl, Jasmin Kappes, Anshuman Chauhan, Hermann Nirschl, Experimental & simulative assessment of mixing quality for dry Li-Ion cathode production in an Eirich intensive mixer, Powder Technol. 431 (2024) 119072.

[22] Bastian Georg Westphal, Nils Mainusch, Chris Meyer, Wolfgang Haselrieder, Maira Indrikova, Paul Titscher, Henrike Bockholt, Wolfgang Viöl, Arno Kwade, Influence of high intensive dry mixing and calendering on relative electrode resistivity determined via an advanced two point approach, J. Energy Storage 11 (2017) 76–85.

[23] Sanghyuk Lim, Sunhyung Kim, Kyung Hyun Ahn, Seung Jong Lee, The effect of binders on the rheological properties and the microstructure formation of lithium-ion battery anode slurries, J. Power Sources 299 (2015) 221–230.

[24] Ernest Jun Jie Tang, Rodney Chua, Yi Cai, Yuqi Guo, Wei How Chong, Suminto Winardi, Tanto Soh, Richa Chaudhary, Madhavi Srinivasan, Rheological studies of $LiNi_{0.6}\ Mn_{0.2}\ Co_{0.2}\ O_2$-based slurry for the development of energy dense li-ion applications, J. Electrochem. Soc. 171 (2) (2024) 020518.

[25] Gyori Park, Jun-Seob Park, Hyun-Suk Kim, Kyung Jin Lee, Preparation of cathode slurry for lithium-ion battery by three-roll mill process, Carbon Lett. 32 (1) (2022) 265–272.

[26] Ming Wang, Dingying Dang, Andrew Meyer, Renata Arsenault, Yang-Tse Cheng, Effects of the mixing sequence on making lithium ion battery electrodes, J. Electrochem. Soc. 167 (10) (2020) 100518.

[27] Eiji Hayakawa, Hideya Nakamura, Shuji Ohsaki, Satoru Watano, Dry mixing of cathode composite powder for all-solid-state batteries using a high-shear mixer, Adv. Powder Technol. 33 (8) (2022) 103705.

[28] C.R.K. Windows-Yule, J.P.K. Seville, A. Ingram, D.J. Parker, Positron emission particle tracking of granular flows, Annu. Rev. Chem. Biomol. Eng. 11 (1) (2020) 367–396.

[29] C.R.K. Windows-Yule, M.T. Herald, A.L. Nicuşan, C.S. Wiggins, G. Pratx, S. Manger, A.E. Odo, T. Leadbeater, J. Pellico, R.T.M. de Rosales, A. Renaud, I. Govender, L.B. Carasik, A.E. Ruggles, Tz Kokalova-Wheldon, J.P.K. Seville, D.J. Parker, Recent advances in positron emission particle tracking: a comparative review, Rep. Progr. Phys. 85 (1) (2022) 016101.

[30] Clemens Lischka, Hermann Nirschl, Simulation of an intensive lab mixer for dry mixing of Li-ion cathode materials via the discrete element method, Particuology (2025).

[31] Mark Al-Shemmeri, Kit Windows-Yule, Estefania Lopez-Quiroga, Peter J. Fryer, Coffee bean particle motion in a spouted bed measured using Positron Emission Particle Tracking (PEPT), J. Food Eng. 311 (2021) 110709.

[32] Katie Cole, Pablo R. Brito-Parada, Kathryn Hadler, Diego Mesa, Stephen J. Neethling, Alexander M. Norori-McCormac, Jan J. Cilliers, Characterisation of solid hydrodynamics in a three-phase stirred tank reactor with positron emission particle tracking (PEPT), Chem. Eng. J. 433 (2022) 133819.

[33] Christopher R.K. Windows-Yule, Roberto Hart-Villamil, Thomas Ridout, Tzany Kokalova, Jose C. Nogueira-Filho, Positron emission particle tracking for liquid-solid mixing in stirred tanks, Chem. Eng. Technol. 43 (10) (2020) 1939–1950, _eprint: https://onlinelibrary.wiley.com/doi/pdf/10.1002/ceat.202000177.

[34] Domenico Daraio, Jose Villoria, Andrew Ingram, Alessio Alexiadis, E. Hugh Stitt, Michele Marigo, Validation of a discrete element method (DEM) model of the grinding media dynamics within an attritor mill using positron emission particle tracking (PEPT) measurements, Appl. Sci. 9 (22) (2019) 4816.

[35] D. Werner, H. Davison, E. Robinson, J.A. Sykes, J.P.K. Seville, A. Wellings, S. Bhattacharya, D.A. Sanchez Monsalve, Tz. Kokalova Wheldon, C.R.K. Windows-Yule, Effect of system composition on mixing in binary fluidised beds, Chem. Eng. Sci. 271 (2023) 118562.

[36] Kit Windows-Yule, Leonard Nicuşan, Matthew T. Herald, Samuel Manger, David Parker, Positron Emission Particle Tracking: A Comprehensive Guide, IOP Publishing, 2022.

[37] Christopher Windows-Yule, Aurelien Neveu, Calibration of DEM simulations for dynamic particulate systems, Pap. Phys. 14 (2022) 140010.

[38] Roberto Hart-Villamil, Andy Ingram, Christopher Windows-Yule, Santoshkumar Gupta, Andrei L. Nicuşan, On the autonomous validation and comparison of particle models for a Newtonian laminar flow mixing model using PEPT, Chem. Eng. Res. Des. 206 (2024) 139–150.

[39] Hanqiao Che, Dominik Werner, Jonathan Seville, Tzany Kokalova Wheldon, Kit Windows-Yule, Evaluation of coarse-grained CFD-DEM models with the validation of PEPT measurements, Particuology 82 (2023) 48–63.

[40] Jack Alan Sykes, Daniel Weston, Niklas Adio, Hanqiao Che, Roberto Hart-Villamil, Andrei Leonard Nicuşan, William Peace, Daniel Rhymer, Dominik Werner, Tzany Kokalova-Wheldon, Andrew Ingram, Christopher R.K. Windows-Yule, Validation of simulations of particulate, fluid and multiphase systems using positron emission particle tracking: A review, Particuology (2024).

[41] David J. Parker, Xianfeng Fan, Positron emission particle tracking—Application and labelling techniques, Particuology 6 (1) (2008) 16–23.

[42] Matthew Herald, Tzany Wheldon, Christopher Windows-Yule, Monte Carlo model validation of a detector system used for Positron Emission Particle Tracking, Nucl. Instrum. Methods Phys. Res. Sect. A: Accel. Spectrometers, Detect. Assoc. Equip. 993 (2021) 165073.

[43] D.J. Parker, R.N. Forster, P. Fowles, P.S. Takhar, Positron emission particle tracking using the new Birmingham positron camera, Nucl. Instrum. Methods Phys. Res. Sect. A: Accel. Spectrometers, Detect. Assoc. Equip. 477 (1) (2002) 540–545.

[44] A.L. Nicuşan, C.R.K. Windows-Yule, Positron emission particle tracking using machine learning, Rev. Sci. Instrum. 91 (1) (2020) 013329.

[45] S.D. Hare, D. Werner, C.R.K. Windows-Yule, T.Z. Kokalova Wheldon, E. Kendrick, M.J.H. Simmons, Use of positron emission particle tracking to assess mixing of a graphite-based lithium-ion anode slurry in an Eirich mixer, Chem. Eng. Res. Des. 197 (2023) 509–518.

[46] Universal Post Processor for Particulate Processes - The Documentation — up4 v0.1.0.dev Manual.

[47] R.D. Wildman, J.M. Huntley, J.-P. Hansen, D.J. Parker, D.A. Allen, Single-particle motion in three-dimensional vibrofluidized granular beds, Phys. Rev. E 62 (3) (2000) 3826–3835.

[48] T.W. Martin, J.P.K. Seville, D.J. Parker, A general method for quantifying dispersion in multiscale systems using trajectory analysis, Chem. Eng. Sci. 62 (13) (2007) 3419–3428.

[49] P.A. Cundall, O.D.L. Strack, A discrete numerical model for granular assemblies, Géotechnique (1979).

[50] A.P. Herman, J. Gan, Z. Zhou, A. Yu, Discrete particle simulation for mixing of granular materials in ribbon mixers: A scale-up study, Powder Technol. (2022).

[51] G.R. Chandratilleke, K.J. Dong, Y.S. Shen, DEM study of the effect of blade-support spokes on mixing performance in a ribbon mixer, Powder Technol. 326 (2018) 123–136.

[52] M. Halidan, G.R. Chandratilleke, K.J. Dong, A.B. Yu, Mixing performance of ribbon mixers: Effects of operational parameters, Powder Technol. 325 (2018) 92–106.

[53] Xin Jin, Shuai Wang, Yansong Shen, DEM study of the effect of impeller design on mixing performance in a U-shape ribbon mixer, Adv. Powder Technol. 33 (1) (2022) 103334.

[54] Xin Jin, Shuai Wang, Yansong Shen, DEM study of mixing behaviours of cohesive particles in a U-shaped ribbon mixer, Powder Technol. 399 (2022) 117097.

[55] Yoshiharu Tsugeno, Mikio Sakai, Sumi Yamazaki, Takeshi Nishinomiya, DEM simulation for optimal design of powder mixing in a ribbon mixer, Adv. Powder Technol. 32 (5) (2021) 1735–1749.

[56] Wei Gao, Lei Liu, Zechu Liao, Shunhua Chen, Mengyan Zang, Yuanqiang Tan, Discrete element analysis of the particle mixing performance in a ribbon mixer with a double U-shaped vessel, Granul. Matter 21 (1) (2019) 12.

[57] Shahab Golshan, Bruno Blais, Insights into granular mixing in vertical ribbon mixers, Can. J. Chem. Eng. 99 (7) (2021) 1570–1581.

[58] Yasunobu Kaneko, Takeo Shiojima, Masayuki Horio, Numerical analysis of particle mixing characteristics in a single helical ribbon agitator using DEM simulation, Powder Technol. 108 (1) (2000) 55–64.

[59] Huaiyuan Qian, Rui Tan, Bei Wu, Fangping Xie, Dawei Liu, Tianci Huang, Qingmiao Xiang, Enhancing mixing efficiency and homogeneity by combining anchor and helical ribbon agitators, Powder Technol. 455 (2025) 120767.

[60] Siyu Wang, Kai Wu, Jiajun Yu, Huiyan Zhang, Design optimization and scale-up characteristics of a double-helical ribbon reactor for biomass catalytic pyrolysis, Powder Technol. 399 (2022) 117192.

[61] Behrooz Jadidi, Mohammadreza Ebrahimi, Farhad Ein-Mozaffari, Ali Lohi, Effect of the mixer design parameters on the performance of a twin paddle blender: A DEM study, Processes 11 (3) (2023).

[62] Ali Hassanpour, Hongsing Tan, Andrew Bayly, Prasad Gopalkrishnan, Boonho Ng, Mojtaba Ghadiri, Analysis of particle motion in a paddle mixer using discrete element method (DEM), Powder Technol. 206 (1) (2011) 189–194, 9th International Symposium on Agglomeration and 4th International Granulation Workshop, 2009.

[63] Mohammadreza Ebrahimi, Amirsalar Yaraghi, Behrooz Jadidi, Farhad Ein-Mozaffari, Ali Lohi, Assessment of bi-disperse solid particles mixing in a horizontal paddle mixer through experiments and DEM, Powder Technol. 381 (2021) 129–140.

[64] Jeroen Emmerink, Ahmed Hadi, Jovana Jovanova, Chris Cleven, Dingena L. Schott, Parametric analysis of a double shaft, batch-type paddle mixer using the discrete element method (DEM), Processes 11 (3) (2023).

[65] S. Garneoui, P. Korzenszky, I. Keppler, Enhancement of the mixture quality of corn grains in a single-shaft paddle mixer using DEM simulations, J. Mech. Sci. Technol. 37 (2023) 1365–1373.

[66] Defu Wang, Jiaqi Yu, Zhijun Lv, Yanhui Song, Huinan Huang, Hui Tian, Haibo Wang, Baohao Su, Effect of impeller rotational speed and paddle angle on binary mixing in a paddle mixer based on DEM, Particuology 102 (2025) 178–189.

[67] Amirsalar Yaraghi, Mohammadreza Ebrahimi, Farhad Ein-Mozaffari, Ali Lohi, Mixing assessment of non-cohesive particles in a paddle mixer through experiments and discrete element method (DEM), Adv. Powder Technol. 29 (11) (2018) 2693–2706.

[68] Veerakiet Boonkanokwong, Rohan P. Frank, Pavithra Valliappan, Brenda Remy, Johannes G. Khinast, Benjamin J. Glasser, Flow of granular materials in a bladed mixer: Effect of particle properties and process parameters on impeller torque and power consumption, Adv. Powder Technol. 29 (11) (2018) 2733–2752.

[69] Michael T. Castro, Joey D. Ocon, Novel designs of blade mixer impellers from the discrete element method and topology optimization, Chem. Eng. J. 490 (2024) 151863.

[70] Angga Pratama Herman, Jieqing Gan, Aibing Yu, GPU-based DEM simulation for scale-up of bladed mixers, Powder Technol. 382 (2021) 300–317.

[71] Meysam Alian, Farhad Ein-Mozaffari, Simant R. Upreti, Analysis of the mixing of solid particles in a plowshare mixer via discrete element method (DEM), Powder Technol. 274 (2015) 77–87.

[72] Paul W. Cleary, Particulate mixing in a plough share mixer using DEM with realistic shaped particles, Powder Technol. 248 (2013) 103–120, Discrete Element Modelling.

[73] B.F.C. Laurent, P.W. Cleary, Comparative study by PEPT and DEM for flow and mixing in a ploughshare mixer, Powder Technol. 228 (2012) 171–186.

[74] Yaohua Zhu, Yan Li, Xinbo Chen, Structure optimization of mixer ploughshare through orthogonal experiment based on DEM simulation, ITM Web Conf. 47 (2022) 02048.

[75] J. Moreno-Juez, L.M. Tavares, R. Artoni, R.M. de Carvalho, E.R. da Cunha, B. Cazacliu, Simulation of the attrition of recycled concrete aggregates during concrete mixing, Materials (2021).

[76] C. Tokoro, T. Yamashita, H. Kubota, S. Owada, Application of DEM simulation to an intensive mixer, Resour. Process. (2009).

[77] H. Hertz, Über die Berührung fester elastischer Körper, J. Für Die Reine Und Angew. Math. 92 (1881).

[78] R.D. Mindlin, H. Deresiewicz, Elastic spheres in contact under varying oblique forces, J. Appl. Phys. (1953).

[79] K.L. Johnson, K. Kendall, A.D. Roberts, Surface energy and the contact of elastic solids, Proc. R. Soc. A: Math. Phys. Eng. Sci. (1971).

[80] E.J.R. Parteli, J. Schmidt, C. Blümel, K.-E. Wirth, W. Peukert, T. Pöschel, Attractive particle interaction forces and packing density of fine glass powders, Sci. Rep. (2014).

[81] T. De, J. Chakraborty, J. Kumar, A. Tripathi, M. Sen, W. Ketterhagen, A particle location based multi-level coarse-graining technique for discrete element method (DEM) simulation, Powder Technol. (2022).

[82] A. Di Renzo, E.S. Napolitano, F.P. Di Maio, Coarse-grain DEM modelling in fluidized bed simulation: A review, Processes (2021).

[83] D. Queteschiner, T. Lichtenegger, S. Pirker, S. Schneiderbauer, Multi-level coarse-grain model of the DEM, Powder Technol. (2018).

[84] C.R. Kit Windows-Yule, Sofiane Benyahia, Peter Toson, Hanqiao Che, A. Leonard Nicuşan, Numerical modelling and imaging of industrial-scale particulate systems: A review of contemporary challenges and solutions, KONA Powder Part. J. 42 (2025) 15–36.

[85] C. Lischka, H. Nirschl, Calibration of li-ion cathode materials for discrete element method simulations, Energy Technol. (2023).

[86] S.A. Morsi, A.J. Alexander, An investigation of particle trajectories in two-phase flow systems, J. Fluid Mech. (1972).

[87] Charles S. Campbell, Granular material flows – an overview, Powder Technol. 162 (3) (2006) 208–229.

[88] P.M.C. Lacey, Developments in the theory of particle mixing, J. Appl. Chem. 4 (5) (1954) 257–268, _eprint: https://onlinelibrary.wiley.com/doi/pdf/10.1002/jctb.5010040504.